Electronic and Magnetic Properties of Transition Metal-Doped MoS_2 Monolayer: First-Principles Calculations

*Dennis Boakye, Henry Martin, Linus K. Labik, Akyana Britwum, Oswald Ashirifi Nunoo, Van W. Elloh, Bright Kwakye-Awuah, Abu Yaya, and Eric K. K. Abavare**

Density functional theory in the framework of generalized gradient approximation (GGA) of Perdew–Burke–Ernzerhof to investigate the effects of some selected transition metal (TM) and rare-earth metal (RE) dopants on the electronic and magnetic properties of a 2D molybdenum disulfide (MoS_2) monolayer is reported. The results demonstrate that it is energetically stable to incorporate Ni and Cu in MoS_2 structure under Mo-rich conditions. The pristine MoS_2 monolayer has a calculated direct bandgap of 1.70 eV and experiences significant reduction in the gap due to the defects. There is observed induced magnetic behavior due to the tight binding effect originating from the localized dopants and the nearest-neighbor Mo atoms, with magnetic moments ranging between 0.82 and 3.00 μ_B. Some of the dopants result in 100% spin polarization which is useful for engineering spin filter devices on magnetic MoS_2 nanostructures.

1. Background

The recent research in 2D materials has attracted a lot of interest because of their promising electrical, mechanical, sensing, optical properties[1] for novel electronic and optoelectronic device application. Since the successful exfoliation of graphene by Geim and Novoselov, a first successful 2D carbon allotrope has broadly been investigated due to its superior electronic, optical, and mechanical properties,[2–5] which has given birth to research in several other related 2D materials. Among these many interesting studies, the ultimate emphasis has been on the manipulation of its atomistic, mechanical, and defect properties, which serve as a basis for design of new novel device applications. Graphene, despite its layered structure, possesses an extraordinary strength compared with its bulk.[6] The transition metal dichalcogenides (TMDCs) (TX_2: where X = chalcogen) are another class of atomically thin 2D materials having a hexagonal structure with a finite bandgap, unlike pristine graphene with a zero bandgap[7] which cannot be used for the fabrication of any logical circuits because of its closed Dirac point. This group includes compounds like tungsten diselenide(WS_2) with recent reported rapid synthesis of GaS and GaSe by Late's group[8] and other layered materials reviewed by Singh[9] and colleagues; however, the overarching merit stems from the high surface-to-volume ratio these materials have and their unique electrical, mechanical, magnetic, and optical properties. However, it should be noted that, among all TMDCs, MoS_2 exhibits superior optoelectronic and catalytic properties compared to the conventional semiconductors[9] materials. A 2D MoS_2 monolayer has unique properties that are applicable in superlubricity, hydrogen production, catalysis, sensing, photovoltaic cells, and biomedicine with still rising potential uses .[10–17] MoS_2 in its available forms exists as a stratified structure with planes of sulfide ions sandwiching planes of molybdenum atoms. These three layers combine to form a single MoS_2 monolayer. The bulk of MoS_2 consists of monolayers which are weakly stacked together by Van der Waals interactions.[18] The bulk phase has an indirect bandgap of 1.20 eV[19] while the single layer has a direct bandgap of 1.80 eV[20] opening the possibilities for the fabrication of switchable transistors.[21] MoS_2 has been predicted to have a better mechanical resonance behavior than graphene, making it a good contender as nanoresonators for highly ultrasensitive mass sensing and detection[22,23] material. We note that MoS_2 has a finite bandgap[24] and therefore a semiconductor which is more desirable compared with semimetal graphene in terms of applications such as optoelectronics, transistors, energy harvesting, and other important areas of nanomaterials. However, by combining these materials' photodetection sensitivities' properties together, their heterostructures can be formed in creating ultrafast photodetectors.[25] MoS_2 has been successfully synthesized through the use of chemical vapor deposition techniques.[26] Monolayer MoS_2 is nonmagnetic, and it has been reported that using electron beam-mediated substitutional doping, TM can alter the electronic and magnetic properties of MoS_2 monolayer.[27,28] Induced magnetization has also been reported by Majid and collaborators[29] by doping RE metals in MoS_2 matrix and

---

D. Boakye, H. Martin, L. K. Labik, A. Britwum, O. A. Nunoo,
B. Kwakye-Awuah, E. K. K. Abavare
Department of Physics
Kwame Nkrumah University of Science and Technology
Kumasi, Ghana
E-mail: eabavare@yahoo.com

V. W. Elloh
Department of Biomedical Engineering
Koforidua Technical University
Koforidua, Ghana

A. Yaya
Department of Materials Science and Engineering
University of Ghana
Legon, Ghana

The ORCID identification number(s) for the author(s) of this article can be found under https://doi.org/10.1002/pssb.202200337.

DOI: 10.1002/pssb.202200337

studied its corresponding atomic and electronic properties. Vacancy defects have also been found to induce magnetic properties under molybdenum-rich conditions extending the magnetic applications of MoS_2.[30] In practice, the TM-doped MoS_2 and vacancy creations are promising ways to extend the potential applications of MoS_2. This is crucial for spin modulators and orientation sensors in spintronic device applications.

To the best of our knowledge, the collective effect of localized single-atom substitutional doping and vacancy defects in MoS_2 has not been studied from the theoretical point of view. Previous studies have only reported either half-metallic properties from each defect, which have practical applications as spin filters in spin transport electronics. However, in this work, we examine the combined effect of both localized (TM = V, Ni, Fe Cu, Mn and RE = Gd, Er, Ce, Nd and La) vacancies and defects on the electronic and magnetic properties of monolayer MoS_2 using quantum mechanical approach in the frame work of first-principles calculations and believe the new results will help further spur research in this material. The work is grouped in sections as follows: 1) background, 2) computational methodologies, 3) results and discussion, and 4) conclusion and acknowledgment.

2. Calculation

We carried out spin-polarized electronic structure calculations based on density functional theory, Hohenberg–Kohn[31,32] formalism as implemented in the Quantum Espresso package[33–35] with its standard pseudopotentials dataset. The nuclei and core electrons interactions are described by the Vanderbilt Ultrassoft pseudopotential (USPP)[36] which considerably reduces the number of plane waves required for the convergence limit. The exchange-correlation effects of the many-body electron–electron interactions are described within the generalized gradient approximation (GGA) of the Perdew–Burke–Ernzerhof (PBE) parameterization[37] and included for all species, nonlinear partial core corrections. We use plane waves expansion for the wavefunction and valence electron density accordingly and solve for the Kohn–Sham orbitals using Davidson iterative diagonalization scheme in the framework of the pseudopotential method. The charge density is updated by modified Broyden[38] prescription. We determined plane wave kinetic energy systematically and found it to be 60 Ry after testing to confirm it was sufficient to assure the accuracy of the calculations with total energy difference among relaxed geometries as 1.30 meV. The Brillouin zone is sampled at a gamma point with k-point mesh density corresponding to 5 × 5 × 1 Monkhorst–Pack grid of the supercell. We apply Gaussian smearing technique with degauss value of 0.1 eV and use Broyden–Fletcher–Goldfarb–Shanno (BFGS)[39] optimization algorithm with all structures fully relaxed until the Hellman–Feynman forces on each atom are less than $0.03\,eV\,Å^{-1}$. Using the calculated lattice constant, all internal coordinates were allowed to relax during optimization procedure. For self-consistent and single-point calculations, the band dispersion is taken along the high-symmetry points of the hexagonal Brillouin zone.

The bulk phase of MoS_2 has a hexagonal crystal structure with $P6_3/mmc$ space group symmetry. Weakly van der Waals forces between intrabond and interbond layers of S—Mo—S exist in this material. The (001) surface of a bilayer unit cell of MoS_2 was chosen to obtain the unit cell[40] and used to model the structure. After careful testing, sufficient 15 Å vacuum thickness was introduced along z-direction of the supercell to prevent structural image interactions as a result of periodic boundary conditions.[41] The supercell was constructed with repeated slab model of the unit cell along the x–y plane using 5 × 5 × 1, as shown in **Figure 1** to simulate a more realistic diluted system. The two adjacent defects are separated over about 16 Å distance due to the size of the supercell to avoid artificial Coulumbic interaction between the defects sites.[42] The extended cell contains 75 atoms with 25 molybdenum (Mo) and 50 sulfur (S) atoms. Each Mo

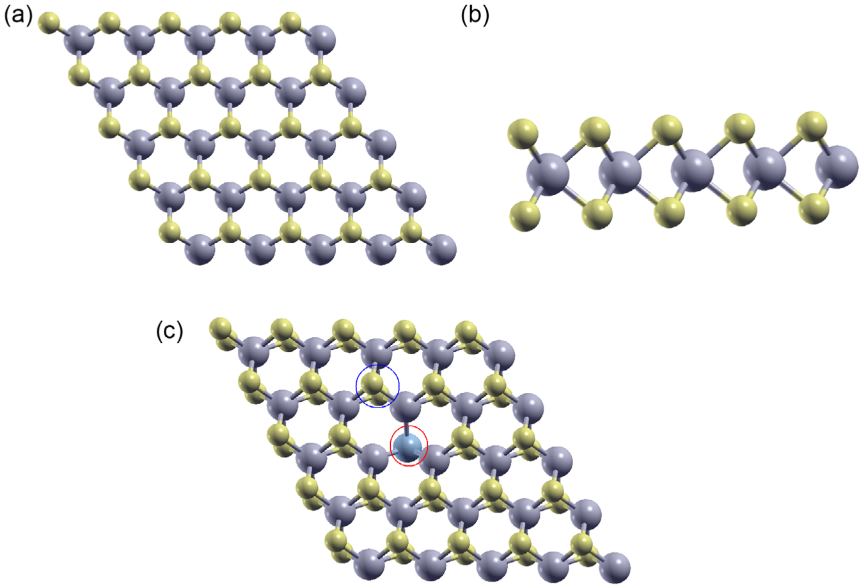

Figure 1. Cyan and yellow stick and balls indicate Mo and S. a) Top and b) side view of 5 × 5 MoS_2 pristine monolayer supercell. c) Red and blue circles are defect and reference regions.

atom has six nearest neighbor S atoms, and each S atom has three nearest Mo atoms bonded to two S atoms to form a hexagonal honeycomb structure. The defects were introduced in the form of substitution of two sulfur atoms with a single TM atom, as shown in Figure 1c. The single-dopant atom generates localized impurity states that increase the effects of electron–hole recombination above the Fermi level.[43] The doping concentration is expressed as a percentage of the number of atoms removed or substituted divided by the total number of S atoms. We find that results from previous studies suggest that the vacancy formation energy of S is much lower than that of Mo according to Rai's group[44] contrary to that reported by Obodo.[45]

We analyzed the structural stability of the defect formation by calculating the formation energy as

$$E_{\text{form}} = E_{\text{dop}} - E_{\text{sup}} - \mu_{\text{d}} + 2\mu_{\text{s}} \tag{1}$$

where the symbols E_{dop}, E_{sup}, μ_{d}, and μ_{s} refer to the total energies of the doped and pristine supercells and the chemical potential of the dopant and sulfur atoms, respectively. The chemical potentials of the elements were computed using the stable phase of each element.

3. Results and Discussions

3.1. Geometry and Stability

We determine the optimized lattice parameter and equilibrium volume for MoS_2 monolayer unit cell as $a = b = 3.182$ Å, and 103.61 $Å^3$, respectively. This is in agreement with previous investigations of theoretical and experimental works.[46,47] The bond distance and angles between molybdenum and sulfur for the pristine structure are also in good agreement with other previous results.[47–49] The Mo—S bond length for the doped structures differs slightly from the pristine structure, as shown in **Table 1**. This observation may be related to the inward relaxation due to the presence of vacancy and dopant atom. Similarly, we study the structural stability of the system based on formation energy and defined it as the energy cost of forming the defect of the doped structure. The defect formation energies of the doped structures are calculated using Equation (1) with results shown in Table 1. Energetically, the lower the defect formation energy, the more structurally stable the system becomes; hence, Ni- and Cu-doped MoS_2 show the most stable structure compared with other dopants consistent with the recent report of Obodo and co-workers.[45]

Table 1. Fully relaxed MoS_2-doped structure with calculated atomic distances (in Å), bond angles (in deg.), and defect formation energy (eV).

System	Mo–S	S–S	Mo–D	S–Mo–S	Mo–D–Mo	Formation energy
Pure	2.412	3.125	–	80.755	–	–
V	2.408	3.122	2.474	80.629	76.396	5.795
Ni	2.410	3.119	2.519	80.652	74.959	−4.383
Fe	2.409	3.120	2.499	80.674	74.959	4.374
Cu	2.410	3.119	2.606	80.662	70.346	−1.246
Mn	2.410	3.118	2.590	80.652	71.432	6.440
Gd	2.410	3.115	2.928	80.526	61.858	4.309
Ne	2.409	3.113	3.010	80.517	59.747	4.0495
La	2.410	3.115	3.070	80.515	58.325	3.714
Ce	2.410	3.115	3.068	80.544	58.429	3.566

3.2. Electronic and Band Dispersion Properties

The pristine MoS_2 monolayer is a direct-bandgap semiconductor. We examined spin-polarized effects of vacancy and substitutional dopants in the electronic properties of MoS_2 monolayer using some selected TM elements, RE metals, and calculated the doped structures of band dispersions, as shown in **Figure 2**, and the corresponding bandgap is given in **Table 2** for the defects electronic behavior. In Figure 2a, it is apparent that the pure MoS_2 monolayer shows semiconductor behavior with the calculated direct bandgap of 1.70 eV and that the conduction band minimum (CBM) and the valence band maximum (VBM) all coincide at the *K*-high symmetry point, in good agreement with other previous study.[20] However, it should be noted that the calculated bandgap in this work suffers from the inherent limitations of GGA's ability to inaccurately describe bandgaps of semiconducting materials due to the lack of the exact description of the exchange-correlation functional but not the topological features of the bands. The band structures for Cu-and Fe-doped MoS_2 are similarly shown in Figure 2b,c. The bandgaps are found to be 1.13 eV and 1.11 eV, respectively. It is observed that impurity energy states are found below the conduction band and above the Fermi level. These flat impurity bands introduced inside the bandgaps are due to the atomic vacancy and are consistent with previous results obtained by Yue and colleagues' group for Cu doping.[41] It is observed that the Fermi levels for both doped structures are shifted upward into the conduction band and are nearly degenerate, making them n-type semiconductor. However, the Cu dopant of MoS_2 exhibits a half-metallic character of spin-up state while the spin down changes to an indirect semiconductor which is consistent with the previous DFT calculation by Obodo and collaborators.[45] As a result, any electron passing through this material would be polarized in the spin-up state, making it a candidate for spin modulation. Interestingly, the Fe-doped structure of MoS_2 shows half-metallic character but with down-spin state.

The V-doped MoS_2 indicates a direct bandgap of 1.11 eV in the spin-down state, as shown in Figure 2d, but half-metallic character in the spin-up state. This is as a consequence of the introduced defect energy state originating from the dopant at the Fermi level and also shows degenerate character. The defect level is lifted upward in the spin-down and indicates indirect bandgap and is a potential candidate as a spin modulator. The band structure for Mn- and Ni-doped MoS_2 is shown in Figure 2e,f with bandgap values of 1.00 eV and 0.96 eV, respectively. Accordingly, their CBM and VBM occur at the same Γ-high symmetry point with equal spin-up and spin-down states. Due to the sulfur vacancy presence, degenerate flat bands are observed in the conduction and valence bands. The two spin states show the same band structure and bandgap compared to other doped structures. The direct-bandgap character of the bandgap is retained, which is useful for laser and other optical applications.

Following TM doping of MoS_2, similar band structure characteristics for RE doping electronic structure calculations are

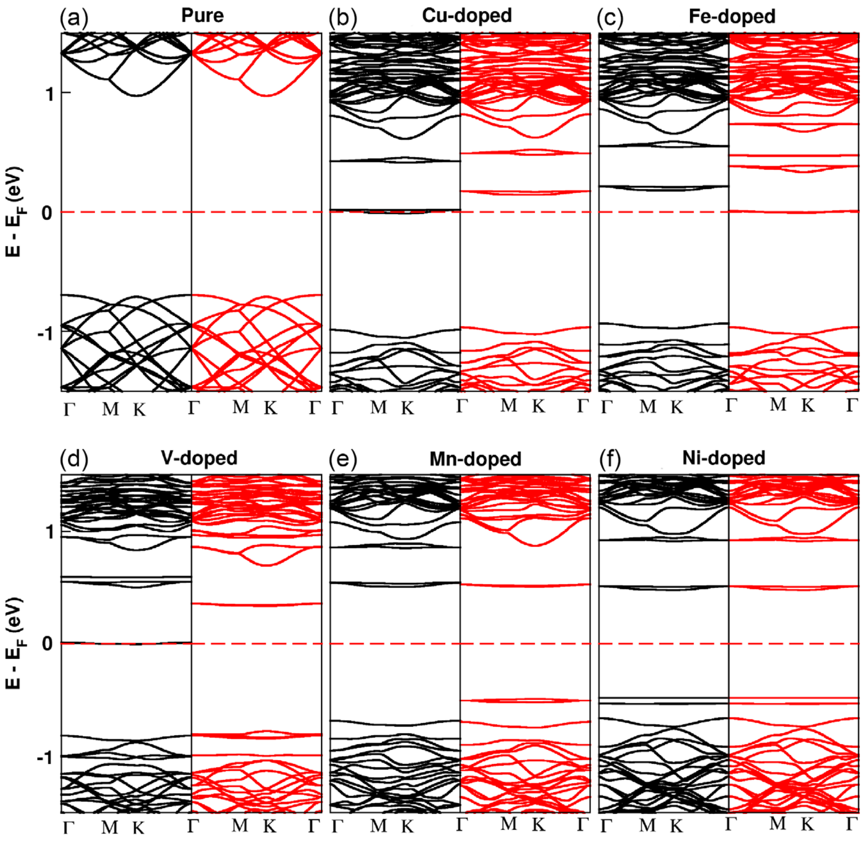

Figure 2. Spin-polarized band structures of a) pristine and b–f) doped defective MoS_2 monolayer. The black and red lines, respectively, represent the spin-up and spin-down dispersive bands, where the Fermi level is set to zero of energy and indicated by red dashed lines.

Table 2. Electronic properties of pure and doped MoS_2.

System	Bandgap [eV]	Nature	Type
Pure	1.70	Semiconductor	Direct
Cu	1.13	Half-metallic	Indirect
Fe	1.11	Half-metallic	Indirect
V	1.11	Half-metallic	Direct
Mn	1.00	Semiconductor	Direct
Ni	0.96	Semiconductor	Direct
Gd	0.79	Half-metallic	Direct
Ce	0.75	Half-metallic	Direct
Ne	0.77	Half-metallic	Direct
La	0.74	Half-metallic	Direct

observed. As shown in **Figure 3**a, the spin-up bands of Gd-doped MoS_2 exhibit semiconducting character with a bandgap of 0.79 eV. However, in Figure 3b, the spin down indicates metallic behavior because of the induced states. This Gd-doped behavior is similar with the remaining RE dopants of Nd, La, and Ce in MoS_2. Table 2 shows the spin-up semiconducting bandgaps of doped Nd, La, and Ce in MoS_2 and those of the selected TM.

We note also that all RE-doped MoS_2 shows a semiconducting direct type of bandgap in the spin-up bands and metallic in the spin-down bands. Codoping of RE and Mn studies was carried out to examine their effect on the band structure and magnetic properties of MoS_2. The results are indicated in **Table 3**. It is clearly seen that there is an increase in the bandgap compared to the single RE dopants. In Figure S4–S7, Supporting Information, we indicate that all the band structures for the codoped MoS_2 of the RE Mn are very similar in topology. The RE-Mn doped MoS_2 is spin up polarized in contrast to the single-RE-doped MoS_2.

The total density of state (TDOS) and projected density of state (PDOS) of the pristine and doped MoS_2 are shown in **Figure 4** accordingly, where the Fermi level is indicated by the red short-dashed line on the energy axis, with both sides of the graph representing valence and conduction bands. It is evident in the structures that, in the pure state, the VBM and CBM are derived primarily from the Mo-4 d and S-3p states, as in Figure 4a. As a consequence, the nonmagnetic character of the pristine MoS_2 is reflected in the symmetric nature of the density of states(DOS) and any modification as a result of the dopants states would lead to new electronic properties. When the pristine MoS_2 is doped with any of the selected dopants, it's seen as impurity which introduces impurity levels near the Fermi level. Following that, it is expected that the electronic property of MoS_2 would be altered due to mixing of electronic orbitals. When Cu is doped, the contribution for half-metallic character is due to the spin-up at the CBM and VBM edges and mainly originates from the

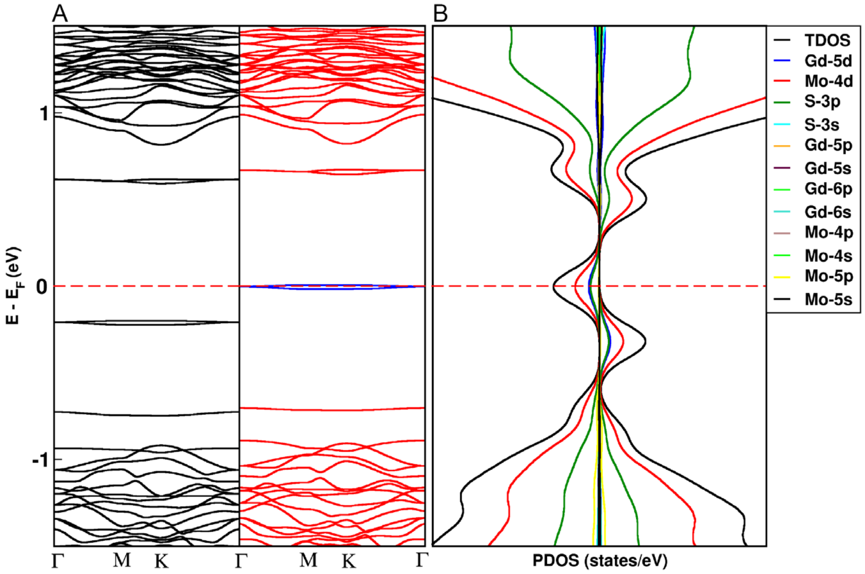

Figure 3. a) Spin-polarized band structure and b) density of states of Gd-doped MoS_2 monolayer. The black and red lines, respectively, represent the spin-up and spin-down dispersive bands, where the Fermi level is set to zero of energy and indicated by red dashed line. Impurity bands are represented by blue lines.

Table 3. Electronic properties of RE Mn-codoped MoS_2.

Codopant	Bandgap [eV]	Nature	Type
Gd–Mn	1.06	Half-metallic	Direct
La–Mn	1.01	Half-metallic	Direct
Nd–Mn	1.05	Half-metallic	Direct
Ce–Mn	1.00	Semiconductor	Direct

mixing of Mo-4 d and S-3p in Figure 4b with negligible contribution from Cu orbitals. However, a closer look at the spin-down states indicates that there are absence of any visible states, further confirming the semiconducting behavior of this state.

A similar behavior is seen for half-metallic character of Fe and Gd dopants but with spin-down state opposite that of Cu-dopant, as in Figure 4c and 3B, respectively. The PDOS contributions come from Fe-3d or Gd-5d and Mo-4d orbitals at the Fermi level, respectively. The spin-up state is clearly seen as the semiconductor because of absence of any state. When V is doped in MoS_2, the PDOS is indicated in Figure 4d. The edges of the valence and conduction bands indicate half-metallic behavior and primarily due to spin-up states with the hybridization of V-3d, S-3p, and Mo-4 d orbitals as the main contributor to the impurity states at the Fermi level. The spin-down state is clearly marked with semiconducting behavior. For Mn and Ni doping, as shown in Figure 4e,f, the edges of the spin-down component are similarly due to the hybridization of Mo-4d, S-3p, and Mn-3 d orbitals. The spin-up component is mainly due to Mo-4d and S-3p orbitals. The Fermi level symmetrically lies in the middle of the conduction and valence bands.

3.3. Magnetic Properties

We perform spin-polarized calculation for the pristine MoS_2 monolayer and show zero magnetic moment, as indicated in **Table 4** and in excellent agreement with known experimental and theoretical values provided by these workers.[48,50] The symmetric appearance of both spin-up and spin-down components in the PDOS distribution in Figure 4a confirms that the monolayer MoS_2 is spin unpolarized and thus has a zero net magnetic moment. The structures of doped MoS_2 have total induced spin magnetic moments of 1.00, 3.00, 2.07, and 0.82 μ_B for V-, Mn-, Fe-, and Cu-doped MoS_2, respectively, while that of Ni-doped MoS_2 has zero net magnetic moment. These results are in excellent agreement with previous studies with Wang's[51] group. In the case of only RE doping, the highest observed magnetic moment is found in Gd with a value of 0.94 μ_B but that increases when codoped with Mn, as indicated in **Table 5**. Among all the dopants, Mn-doped MoS_2 shows the highest magnetic moment. We further studied the distribution of magnetism on the doped structures. The spin-resolved charge density was calculated, as shown in **Figure 5**. The green and blue isosurfaces represent the positive and negative spin densities, respectively. Spin polarization may arise on a dopant and surrounding Mo atoms in the interstitial region near the dopant if asymmetric distribution of spin-up and spin-down charge components exists, which would result in magnetic properties of the structure. The Cu and Gd-doped MoS_2 has the spins of the three nearest Mo atoms parallel to that of the dopant, thereby increasing the total magnetic moment, whereas they are antiparallel in the case of Fe doping and consequently reducing the magnitude of the total magnetic moment. Furthermore, hybridization between the 3 d states of the dopant and p states of the nearest six sulfur atoms results in spin splitting for the sulfur atoms that are antiparallel to the dopant, while the Mo atoms are parallel to the dopant. In the case of V- and Mn-doped MoS_2, the spins of the three nearest sulfur atoms are parallel to the dopant and antiparallel to the three Mo atoms bonded to the dopant.

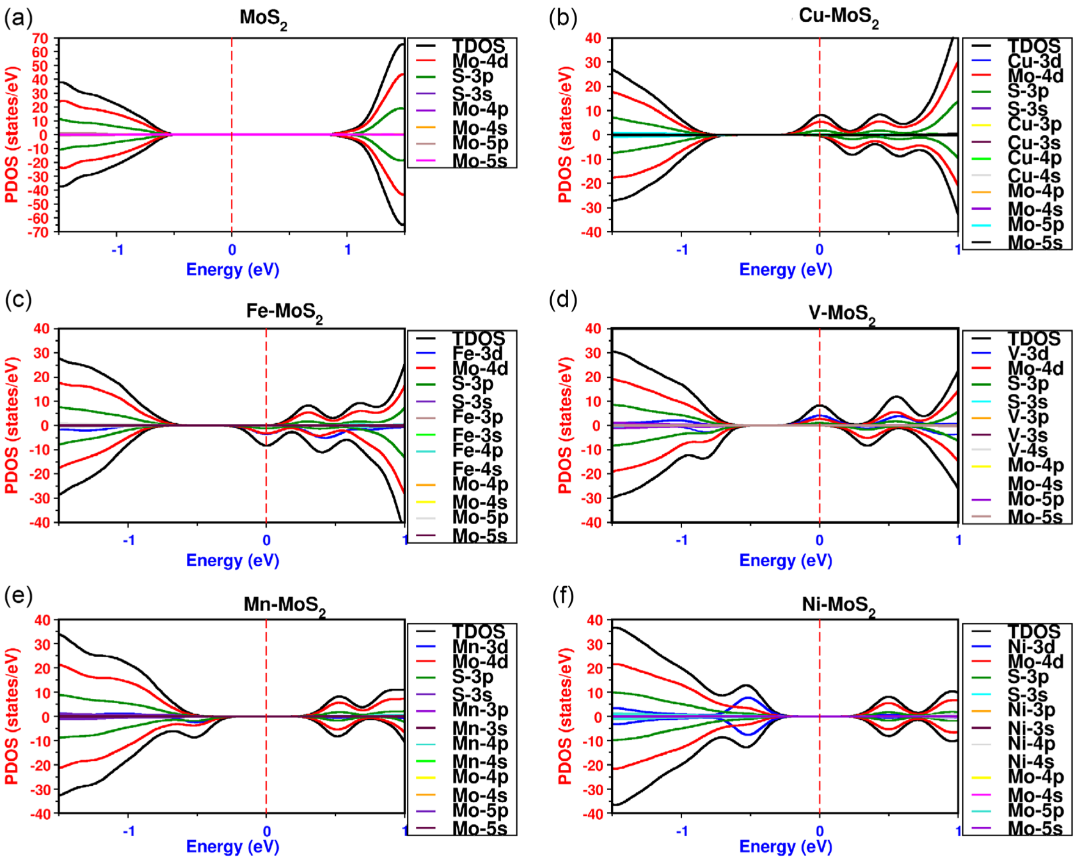

Figure 4. The PDOS of a) pure and b–f) doped structures of MoS$_2$ monolayer. The Fermi level is indicated by the red dashed line.

Table 4. Magnetic moments of pure and doped MoS$_2$.

System	Dopant [μ_B]	Total [μ_B]
Pure	–	0.00
Cu	0.04	0.82
Fe	2.64	2.07
V	0.80	1.00
Mn	3.49	3.00
Ni	0.00	0.00
Gd	0.14	0.94
Ne	0.13	0.92
La	0.12	0.92
Ce	0.13	0.91

Table 5. Magnetic moments of RE–Mn codoping MoS$_2$.

System	Dopant [μ_B]	Total [μ_B]
Gd–Mn	–	2.01
La–Mn	–	2.00
Nd–Mn	–	2.01
Ce–Mn	–	2.01

4. Conclusion

We report density functional theory in the framework of spin-polarized calculation to clarify the electronic and magnetic properties of MoS$_2$ monolayer with TM/RE dopants. The calculated formation energies suggest that it is energetically stable to dope MoS$_2$ monolayer under sulfur-deficient conditions than other dopants, consistent with similar calculations. The bond lengths for Mo—S in the doped structures are slightly lower compared to the pristine material, leading to reduced S–Mo–S bond angles due to inward relaxation of the structures and consequently decreasing monolayer thickness. Band structure calculations for the spin states revealed that pure MoS$_2$ is a direct semiconductor with a bandgap of 1.70 eV, reducing considerably in the doped structures. The direct bandgap changes to indirect in other doped structures. With the exception of Ni-doped MoS$_2$, spin magnetic moments were induced in the doped structures and the highest magnetic moment arising from Mn-doped MoS$_2$. Spin charge density calculations revealed that the three Mo atoms bonded to the dopant are antiparallel to the dopant in Fe, Mn, and V-doped MoS$_2$ but parallel to the dopant in Cu- and RE-doped MoS$_2$ monolayer, resulting in a decrease or increase in the total magnetic moment, respectively. Analysis of the partial density of states for the doped structures revealed that the valence and conduction bands were primarily dominated by the hybridization between 4 d states of Mo, 3p states of S, and the 3d/5d

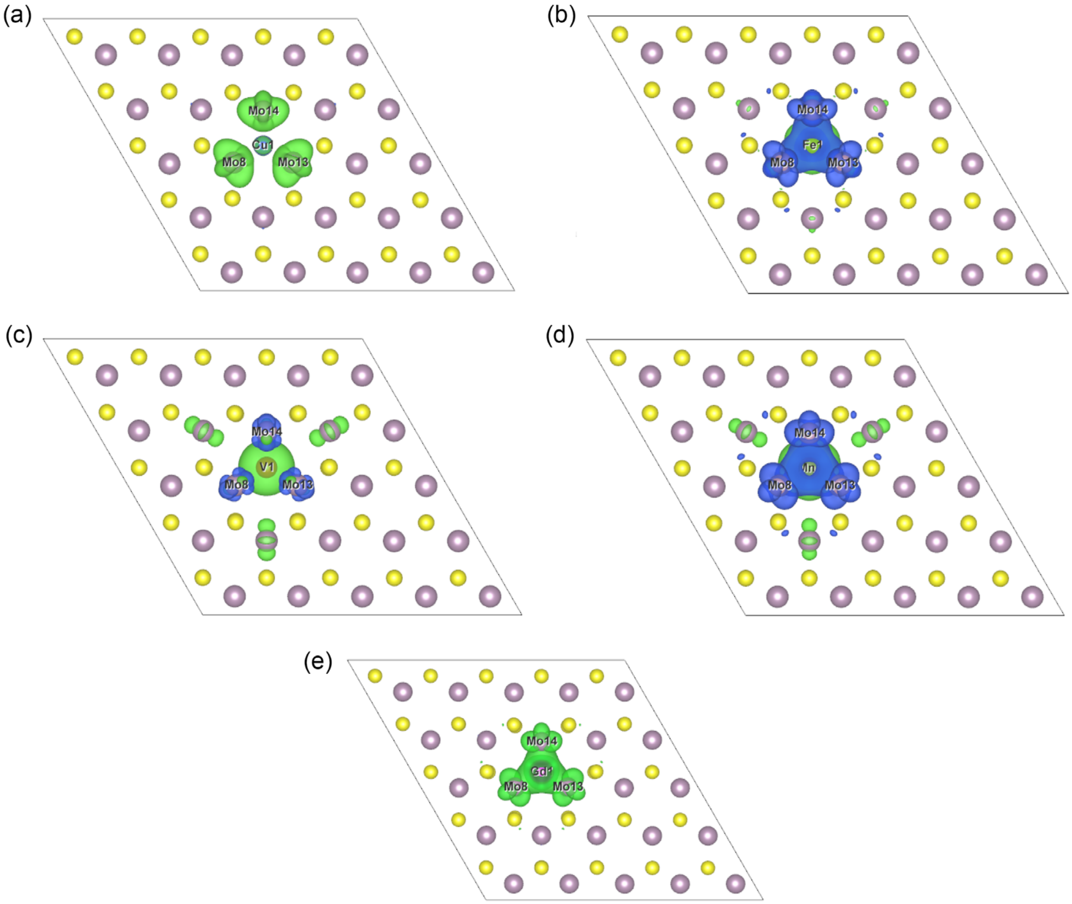

Figure 5. The calculated localized spin density distribution near the Fermi level of a) Cu, b) Fe, c) V, d) Mn, and e) Gd-doped MoS_2 monolayer. The localized charge density is indicated by an isosurface value of 2% of the maximum isovalue $e/Å^3$. Green and blue colors represent spin-up and spin-down charge distribution, respectively.

states of the dopant atoms. Defect energy levels were found at the Fermi energy level for single spin states producing half-metallic structures. Mn-doped MoS_2 produced spin magnetic semiconductors. These spin-polarized structures are useful as spin filters (spin-polarized current) and spin injectors in spintronic applications. The induction of spin magnetic moments makes them useful as nanomagnets in nanorobotics.

Supporting Information

Supporting Information is available from the Wiley Online Library or from the author.

Acknowledgements

The authors acknowledge the use of South African Center for High Performance Computing (CHPC) resources for the computations.

Conflict of Interest

The authors declare no conflict of interest.

Data Availability Statement

The data that support the findings of this study are available from the corresponding author upon reasonable request.

Received: July 22, 2022
Revised: March 27, 2023
Published online: May 10, 2023

[1] D. Er, K. Ghatak, in *Synthesis, Modeling and Characterization of 2D Materials and Their Heterostructures* (Eds: E. H. Yang, D Datta, J. Ding, G. Hader), Elsevier, Amsterdam **2020**, pp. 113–123.
[2] K. Novoselov, A. Geim, S. Morozov, S. Dubonos, Y. Zhang, D. Jiang, arXiv:cond-mat/0410631, **2004**.
[3] A. K. Geim, K. S. Novoselov, in *Nanoscience and Technology: A Collection of Reviews from Nature Journals*, World Scientific, Singapore **2010**, pp. 11–19.
[4] K. S. Novoselov, A. K. Geim, S. V. Morozov, D. Jiang, M. I. Katsnelson, I. Grigorieva, S. Dubonos, A. Firsov, *Nature* **2005**, *438*, 197.
[5] K. S. Novoselov, D. Jiang, F. Schedin, T. Booth, V. Khotkevich, S. Morozov, A. K. Geim, *Proc. Natl. Acad. Sci USA.* **2005**, *102*, 10451.
[6] C. Lee, X. Wei, J. W. Kysar, J. Hone, *Science* **2008**, *321*, 385.

[7] K. F. Mak, C. Lee, J. Hone, J. Shan, T. F. Heinz, *Phys. Rev. Lett.* **2010**, *105*, 136805.

[8] D. J. Late, B. Liu, H. R. Matte, C. Rao, V. P. Dravid, *Adv. Funct. Mater.* **2012**, *22*, 1894.

[9] A. K. Singh, P. Kumar, D. Late, A. Kumar, S. Patel, J. Singh, *Appl. Mater. Today* **2018**, *13*, 242.

[10] B. Hinnemann, P. Moses, J. Bonde, *J. Am. Chem. Soc* **2005**, *127*, 5308.

[11] T. F. Jaramillo, K. P. Jørgensen, J. Bonde, J. H. Nielsen, S. Horch, I. Chorkendorff, *Science* **2007**, *317*, 100.

[12] E. Gourmelon, O. Lignier, H. Hadouda, G. Couturier, J. Bernede, J. Tedd, J. Pouzet, J. Salardenne, *Sol. Energy Mater. Sol. Cells* **1997**, *46*, 115.

[13] Y. Li, H. Wang, L. Xie, Y. Liang, G. Hong, H. Dai, *J. Am. Chem. Soc.* **2011**, *133*, 7296.

[14] H. Wu, R. Yang, B. Song, Q. Han, J. Li, Y. Zhang, Y. Fang, R. Tenne, C. Wang, *ACS Nano* **2011**, *5*, 1276.

[15] M. De, S. Rana, H. Akpinar, O. R. Miranda, R. R. Arvizo, U. H. Bunz, V. M. Rotello, *Nat. Chem.* **2009**, *1*, 461.

[16] L.-P. Feng, Su, J. Su, Z.-T. Liu, *J. Alloys Compd.* **2014**, *613*, 122.

[17] C. Lee, Q. Li, W. Kalb, X.-Z. Liu, H. Berger, R. W. Carpick, J. Hone, *Science* **2010**, *328*, 76.

[18] *Gmelin Handbook of Inorganic and Organometallic Chemistry*, 8th edn. (Eds: P. E. Parthé, L. Gelato, B. Chabot, M. Penzo, K. Cenzual, R. Gladyshevskii), Springer-Verlag, Berlin; Vol. 1: **1993**, pp. 1–260; Vol. 2: **1993**, pp. 261–668; Vol. 3: **1994**, pp. 669–1180; Vol. 4: **1994**, pp. 1181–1596.

[19] W. Zhu, T. Low, Y.-H. Lee, H. Wang, D. B. Farmer, J. Kong, F. Xia, P. Avouris, *Nat. Commun.* **2014**, *5*, 3087.

[20] X. Zhao, C. Xia, T. Wang, X. Dai, *Solid State Commun.* **2015**, *220*, 31.

[21] B. Radisavljevic, A. Radenovic, J. Brivio, V. Giacometti, A. Kis, *Nat. Nanotechnol.* **2011**, *6*, 147.

[22] M. Zhou, Y. Zhai, S. Dong, *Analyt. Chem.* **2009**, *81*, 5603.

[23] X. He, S. Kitipornchai, K. Liew, *Nanotechnology* **2005**, *16*, 2086.

[24] K. Kam, B. Parkinson, *J. Phys. Chem.* **1982**, *86*, 463.

[25] J.-W. Jiang, *Front. Phys.* **2015**, *10*, 287.

[26] K. Zhang, S. Feng, J. Wang, A. Azcatl, N. Lu, R. Addou, N. Wang, C. Zhou, J. Lerach, V. Bojan, M. J. Kim, *Nano Lett.* **2015**, *15*, 6586.

[27] M. Saab, P. Raybaud, *J. Phys. Chem. C* **2016**, *120*, 10691.

[28] X.-L. Fan, Y.-R. An, W.-J. Guo, *Nanoscale Res. Lett.* **2016**, *11*, 154.

[29] A. Majid, A. Imtiaz, M. Yoshiya, *J. Appl. Phys.* **2016**, *120*, 142124.

[30] C. Ataca, S. Ciraci, *J. Phys. Chem. C* **2011**, *115*, 13303.

[31] P. Hohenberg, W. Kohn, *Phys. Rev.* **1964**, *136*, B864.

[32] W. Kohn, L. J. Sham, *Phys. Rev.* **1965**, *140*, A1133.

[33] P. Giannozzi, S. Baroni, N. Bonini, M. Calandra, R. Car, C. Cavazzoni, D. Ceresoli, G. L. Chiarotti, M. Cococcioni, I. Dabo, S. de Gironcoli, S. Fabris, G. Fratesi, R. Gebauer, U. Gerstmann, C. Gougoussis, A. Kokalj, M. Lazzeri, L. Martin-Samos, N. Marzari, F. Mauri, R. Mazzarello, S. Paolini, A. Pasquarello, L. Paulatto, C. Sbraccia, S. Scandolo, G. Sclauzero, A. P. Seitsonen, et al., *J. Phys. Condens. Matter* **2009**, *21*, 395502.

[34] P. Giannozzi, O. Andreussi, T. Brumme, O. Bunau, M. B. Nardelli, M. Calandra, R. Car, C. Cavazzoni, D. Ceresoli, M. Cococcioni, N. Colonna, I. Carnimeo, A. Dal Corso, S. de Gironcoli, P. Delugas, R. A. DiStasio Jr, A. Ferretti, A. Floris, G. Fratesi, G. Fugallo, R. Gebauer, U. Gerstmann, F. Giustino, T. Gorni, J. Jia, M. Kawamura, H.-Y. Ko, A. Kokalj, E. Küçükbenli, et al., *J. Phys.: Condens. Matter* **2017**, *29*, 465901.

[35] S. Scandolo, P. Giannozzi, C. Cavazzoni, S. deGironcoli, A. Pasquarello, S. Baroni, *Z. Kristallogr. Cryst. Mater.* **2005**, *220*, 574.

[36] D. Vanderbilt, *Phys. Rev. B* **1990**, *41*, 7892.

[37] J. P. Perdew, K. Burke, M. Ernzerhof, *Phys. Rev. Lett.* **1996**, *77*, 3865.

[38] D. D. Johnson, *Phys. Rev. B* **1988**, *38*, 12807.

[39] J. D. Head, M. C. Zerner, *Chem. Phys. Lett.* **1985**, *122*, 264.

[40] A. Jain, S. P. Ong, G. Hautier, W. Chen, W. D. Richards, S. Dacek, S. Cholia, D. Gunter, D. Skinner, G. Ceder, et al., *APL Mater.* **2013**, *1*, 011002.

[41] Q. Yue, S. Chang, S. Qin, J. Li, *Phys. Lett. A* **2013**, *377*, 1362.

[42] L. Kantorovich, *Phys. Rev. B* **1999**, *60*, 15476.

[43] S. Cheriyan, D. Balamurgan, S. Sriram, *Superlattices Microstruct.* **2018**, *116*, 238.

[44] D. Rai, T. V. Vu, A. Laref, M. Ghimire, P. Patra, S. Srivastava, *Nano-Struct. Nano-Obj.* **2020**, *21*, 100404.

[45] K. O. Obodo, C. N. M. Ouma, J. T. Obodo, M. Braun, D. Bessarabov, *Comput. Condens. Matter* **2019**, *21*, 00419.

[46] S. Zhao, J. Xue, W. Kang, *Chem. Phys. Lett.* **2014**, *595*, 35.

[47] Y. Jing, X. Tan, Z. Zhou, P. Shen, *J. Mater. Chem. A* **2014**, *2*, 16892.

[48] D. Ma, W. Ju, T. Li, X. Zhang, C. He, B. Ma, Y. Tang, Z. Lu, Z. Yang, *Appl. Surf. Sci.* **2016**, *364*, 181.

[49] A. Hussain, M. Tayyab, *Comput. Condens. Matter* **2020**, *24*, e00494.

[50] S.-C. Lu, J.-P. Leburton, *Nanoscale Res. Lett.* **2014**, *9*, 1.

[51] Q. H. Wang, K. Kalantar-Zadeh, A. Kis, J. N. Coleman, M. S. Strano, *Nat. Nanotechnol.* **2012**, *7*, 699.